An analysis of directivity pulses using empirical data and dynamic rupture simulations of the 2023 Kahramanmaras earthquake doublet

Ming-Hsuan Yen[1,2] (ID), Elif Türker[1,2], Thomas Ulrich[3], Mathilde Marchandon[3], Alice-Agnes Gabriel[3,4], and Fabrice Cotton[1,2]

Abstract

Near-field earthquake ground motions characterized by strong velocity pulses can cause extensive damage to buildings and structures. Such pulses were identified during the Mw 7.8 and Mw 7.5 earthquake doublet of the 2023 Turkey seismic sequence, potentially contributing to the extensive damage it caused. Therefore, a better understanding and characterization of pulse properties (e.g. period and amplitude) and their underlying physical factors are crucial for earthquake-resistant design. In this study, we characterize the velocity pulses reported in observed records and synthetic waveforms generated by a three-dimensional (3D) dynamic rupture simulation of the Mw 7.8 event. We observed significant variability in the pulse properties of the observed records in near-fault regions, particularly regarding their orientations. This variability was not fully captured by the dynamic rupture simulation. Our results indicate that directivity effects are not the only factors influencing pulse characteristics in this earthquake doublet. While site effects (e.g. basin effects) may influence pulse characteristics at some stations, local heterogeneities in slip amplitude, orientations, and fault geometries can be critical in generating or influencing pulse properties in this earthquake doublet.

Keywords

2023 Turkey earthquake, pulse orientation, strong velocity pulses, site effects, directivity effect

Date received: 15 January 2024; accepted: 18 November 2024

[1]German Research Centre for Geoscience GFZ, Potsdam, Germany
[2]Institute of Geosciences, University of Potsdam, Potsdam, Germany
[3]Department of Earth and Environmental Sciences, Ludwig-Maximilians-Universität München, Munich, Germany
[4]Institute of Geophysics and Planetary Physics, Scripps Institution of Oceanography, University of California San Diego, La Jolla, CA, USA

Corresponding author:
Ming-Hsuan Yen, German Research Centre for Geoscience GFZ, Telegrafenberg, 14473 Potsdam, Germany.
Email: ming-hsuan.yen@gfz-potsdam.de

Introduction

The left-lateral East Anatolian Fault Zone (EAFZ) in Turkey extends for more than 550 km, starting from the Karliova Triple Junction in the east to the southernmost end of the Mediterranean Sea (Duman and Emre, 2013). Even though the EAFZ is less seismically active than the North Anatolian Fault Zone, it has hosted numerous large (Mw > 6.5) earthquakes over the last few centuries (Sengör et al., 1985; Tatar et al., 2004), the most recent being the Mw 6.8 Elazig earthquake in 2020.

On 6 February 2023, at 01:17 UTC, a Mw 7.8 earthquake nucleated only 20 km off the main strand of the EAFZ, rupturing multiple segments of the East Anatolian Fault system. Just 9 h later, another major earthquake (Mw 7.5) occurred 90 km north of the first mainshock, on the northern strand of the EAFZ, near Elbistan province. Following these two mainshocks, the region experienced hundreds of aftershocks with Mw > 4. We refer to these two major events as the "earthquake doublet." This doublet caused significant damage to more than 220,000 buildings (which were either totally destroyed or collapsed), resulting in over 55,000 casualties in Turkey and Syria (Hacettepe University Department of Civil Engineering, 2023). Cities located more than 150 km from the epicenter (e.g. Hatay) were completely devastated. Thus, it was the worst disaster that the country has experienced in the last millennium.

Strong velocity pulses have been identified in these earthquakes and correlated with the extensive damage distribution observed (Baltzopoulos et al., 2023; Erdik et al., 2023). These findings align with previous studies of large and moderate earthquakes that demonstrated the potential impact of strong velocity pulses on resulting seismic damage (Heaton et al., 1995; Strasser and Bommer, 2009; Türker et al., 2023).

Such velocity pulses can be generated by two main physical phenomena: fling steps and directivity effects. A fling step is associated with a displacement waveform containing a permanent offset and occurs in very near-surface fault ruptures (Hisada and Tanaka, 2021). It is characterized by a one-sided pulse (fling pulse) in the velocity waveform and a step-function displacement waveform. Directivity pulses result from near-field rupture directivity effects and are observed in the direction of rupture propagation (Bray and Rodriguez-Marek, 2004; Somerville et al., 1997). A directivity pulse is a two-sided pulse in the velocity waveform. However, several studies have commented on the origin of velocity pulses being more complex. Rodriguez-Marek and Bray (2006) showed that site effects can interact with near-field directivity effects when the pulse period is close to the site's dominant frequency. These effects may interact mutually or solely affect pulse generation (Chioccarelli and Iervolino, 2010; Kaneko and Goto, 2022), potentially leading to significant variability in pulse properties. In addition, localized variability arises from dynamic rupture effects, including off-fault plasticity, surface-breaking, or coalescence of multiple rupture fronts due to fault property heterogeneities or geometric complexity (Schliwa and Gabriel, 2023; Wang and Day, 2020).

Most pulse analyses have been conducted using empirical data. However, numerical simulations can also aid a better assessment of the factors controlling pulse variability (Yen et al., 2022). The severe seismic damage and complex rupture process of this seismic sequence in Turkey have inspired numerous studies to understand the earthquake origin and rupture process (Jia et al., 2023; Mai et al., 2023; Petersen et al., 2023). The dynamic rupture models of Jia et al. (2023) and Gabriel et al. (2023), which treat the nucleation, propagation, and arrest of earthquakes in a physically self-consistent manner, independently reproduce the main features of the kinematic models for the Mw 7.8 earthquake

and produce ground motion synthetics that exhibit pulse-like behavior. These simulations provide a valuable opportunity to study the variability of ground motion pulses from synthetic data.

In this study, we analyze pulse variability in detail, in terms of period, velocity amplitude, and orientation. We use the wavelet analysis method of Shahi and Baker (2014) (see the Methodology section) to extract the pulses and characterize their properties. We analyze the characteristics of the observed pulses and those obtained from the simulations of Jia et al. (2023) to comprehensively quantify and evaluate pulse variability. Furthermore, we compare the results with the pulse characteristics obtained in past earthquakes (updated database of Yen et al. (2022)).

Data

For the analysis, we investigate two observed empirical datasets from the Mw 7.8 Pazarcik and Mw 7.5 Elbistan earthquakes, as well as two synthetic datasets from the Mw 7.8 Pazarcik earthquake. These two earthquakes were recorded by 349 and 288 strong ground motion stations (AFAD-TADAS), respectively. The two synthetic datasets are derived from the physics-based three-dimensional (3D) dynamic rupture simulation of Jia et al. (2023).

The first observed empirical data used in this study are initially provided by AFAD-TADAS. We perform the following processing on the raw data: (1) detrending acceleration waveforms, (2) cumulative integration of acceleration waveforms into velocity waveforms, and (3) detrending velocity waveforms. We refer to this dataset as "uncorrected data," indicating that the static displacement in the time history is uncorrected.

The corrected data are provided by the Engineering Strong Motion Database (ESM) (Luzi et al., 2020), which have been manually corrected by the ESM data processing team using the broadband ITACA processing schemes of Paolucci et al. (2011). The processing includes (1) baseline correction (constant detrending), a cosine taper, and a second-order acausal frequency domain Butterworth filter applied to the acceleration time series; (2) double integration of the acceleration time series to obtain the displacement time series; and (3) linear detrending applied to the obtained displacement time series. These processes remove the static displacements in the time history, as shown in the time histories of stations 3123 (in the basin), 3144 (at the center of the rupture fault), 4615 (near the hypocenter), and 4616 (at the intersection of two faults) shown in Figure S1. We refer to this dataset as "corrected data," indicating the removal of the static displacement in the time history.

The two synthetic datasets used in this study are derived from the dynamic rupture simulation of Jia et al. (2023) and are referred to as the first synthetic data and the second synthetic data. The first synthetic dataset is directly from the model of Jia et al. (2023), with a maximum resolved frequency of 1.5 Hz. The second synthetic dataset is derived from a higher resolution dynamic rupture model, based on a larger mesh of 685 million cells and a higher polynomial order of the basic functions ($p = 5$), which was unpublished and required significant supercomputing resources (10 h on the full Frontera supercomputer, equivalent to 4.5 million CPU hours). The simulation is numerically accurate to 5 Hz in an NW-SE aligned refined area of 400 km $\times$ 200 km $\times$ 20 km, containing the fault network and all the near-fault stations. Dynamic rupture models require many assumptions, including the initial fault loading and strength, subsurface velocity model and

geometries, and fault friction. The fault geometry is based on surface rupture traces inferred from available satellite data (e.g. USGS and Sentinel-2), and the initial shear stress is inferred from regional seismo-tectonics with small-scale heterogeneities inferred from static slip inversion. The models incorporate topography. The one-dimensional (1D) velocity model is based on the study of Güvercin et al. (2022) and does not consider heterogeneous site configurations (e.g. Vs30). Such models predict the evolution of slip, seismic waves, and surface deformation in a physically self-consistent manner. The maximum resolved frequency is sufficient for our pulse identification analysis, as pulse periods generally range between 1 and 15 s (0.1–1 Hz), as shown by the pulse scaling by Shahi and Baker (2014) and Yen et al. (2022). Jia et al. (2023) have shown that the surface displacements and slip histories produced by the dynamic rupture simulation compare well with high-resolution geodetic data, kinematic rupture representations, and observed ground motions. We further examine how pulse characteristics and their variability are reproduced by the models. The synthetic time histories of selected stations are shown in Figure S2. The synthetic data processing is carried out in the same manner as for the uncorrected data.

Identification and characterization of velocity pulses

Methodology

In this study, we use the wavelet analysis algorithm of Shahi and Baker (2014) to detect pulse-like velocity in the Kahramanmaraş earthquake doublet. Their wavelet analysis has been widely recognized and used in other studies on this earthquake doublet (Baltzopoulos et al., 2023; Ertuncay and Costa, 2024). This choice ensures consistency with previous studies in the characterization of velocity pulses, particularly the analyses of Shahi and Baker (2014) and Yen et al. (2022).

The algorithm employs the wavelet transform of two horizontal orthogonal components of the ground motion to search for orientations more likely to contain strong pulses. The wavelet with the largest coefficient is identified as the strongest pulse. Thus, the pulse properties in this study reflect the characteristics of the strongest pulse.

The strength of a pulse is classified by the pulse indicator (PI), which defines the strength as follows: (Equation 12 of Shahi and Baker, 2014):

$$
\begin{aligned}
PI &= 9.384(0.76 - PC - 0.0616PGV)(PC + 6.914 \times 10^{-4}PGV - 1.072) - 6.179 \\
PC &= 0.63 \times PGV_{ratio} + 0.777 \times energy_{ratio}
\end{aligned}
\tag{1}
$$

where the principal component (PC) is the linear combination of two variables (peak ground velocity (PGV) of the waveform projected along the extracted orientation ratio and energy ratio), accounting for the largest amount of variability in the data, and the energy ratio is the L2 norm of the residual and original ground motions, while the PGV ratio is that of the residual and original PGV.

As a first criterion for pulse identification, the PGV must exceed 20 cm/s, following the criterion established by Shahi and Baker (2014). The classification algorithm then categorizes a velocity time history as either pulse-like or non-pulse-like, according to the PI value. A record is defined as pulse-like if PI > 0, or as non-pulse-like if PI < 0. The algorithm also provides additional information about the pulse, including its orientation, period (T_p), and the associated PGV.

Velocity pulses from observed empirical data

Following the aforementioned selection criteria (i.e. PGV > 20 cm/s), we selected 50 stations within a rupture distance (R_{rup}) of 250 km for both the observed data (uncorrected and corrected) from the Mw 7.8 Pazarcik earthquake. Similarly, 21 stations within a rupture distance of 200 km were selected for the observed data from the Mw 7.5 Elbistan earthquake. The pulses identified from the corrected data of the Pazarcik earthquake (first event) are present at 23 out of the 50 stations listed in Table 1. The pulses identified for the Elbistan event (second event) are listed in Table 2, with 7 out of the 21 stations indicated as pulses. The rupture distances are calculated from the stations to the rupture models of the earthquake doublet referenced by the United States Geological Survey (USGS).

Figure 1a and Table 1 show the pulse distribution for the observed data of the Mw 7.8 Pazarcik earthquake first event). A noticeable trend is that most of the observed pulses are located along the main fault branch (EAFZ), with 22 out of 23 records having R_{rup} < 20 km (i.e. near-fault). Conversely, the hypocentral distances seem to play a minor role in pulse detection, with highly variable distances ranging from 30 to 130 km (Table 1). The pulse orientations (i.e. fault-normal (FN) or fault-parallel (FP) components) exhibit high variability. The largest pulse PGV (173–179 cm/s) is found at station 3123, located in the city of Antakya (R_{hypo} = 130 km; R_{rup} = 1.5 km), which suffered the most seismic damage during these events.

Figure 1b and Table 2 show the pulse characteristics for the observed data of the Mw 7.5 Elbistan earthquake (second event). Notably, the pulses are mostly located to the south, away from the main fault segment, with R_{rup} ranging from 3 km to almost 70 km. Pulse-like features are detected only at a few stations and at greater distances, likely due to the limited number of stations near the fault. Pulse orientations at stations in the rupture direction are on the FN component (stations 131, 132, and 4612), while those at stations to the south of the fault are on the FP component. The largest pulse PGV (181 cm/s) is recorded at station 4612, marked by R_{rup} = 3 km.

Velocity pulses from synthetic data

First, to ensure that the synthetic recordings exhibit the key features of interest, we compare the time histories of stations 3123 (in the Karasu-Amik Basin), 3144 (at the center of the East Anatolian Fault), 4615 (near the hypocenter), and 4616 (at the intersection of East Anatolian Fault segments) for the uncorrected, corrected, and synthetic data (Figure 2). All their time histories show pulse-like features, confirming that we can analyze the pulses using these synthetic data.

We then apply the pulse extraction algorithm to both generations of the synthetic ground motions. The synthetic data of the Pazarcik event show pulse-like features at 18 out of 50 stations in the first synthetic dataset and at 17 out of 50 stations in the second synthetic dataset (Table 1). The simulations capture specific pulse characteristics, such as pulse period and velocity, at most stations in the near-fault region. However, the pulse orientations show a significant tendency to focus on the FN component in both synthetic datasets (Figure 3a and b).

High-frequency ground motions are not fully modeled by the simulation approach, and false positives of impulsive motions may result from this lack of high frequencies. Table 3 indicates the ratio of pulse-like motions over total stations per distance. The percentages between the number of pulses from empirical data and simulations differ slightly only for

Table 1. Parameters table of the extracted pulses for the Mw 7.8 Pazarcik earthquake

Index	Sta.	R_{hypo} (km)	R_{rup} (km)	Uncorrected data					Corrected data					First synthetic data					Second synthetic data				
				Ang.	Ori.	T_p (s)	PGV (cm/s)	PI	Ang.	Ori.	T_p (s)	PGV (cm/s)	PI	Ang.	Ori.	T_p (s)	PGV (cm/s)	PI	Ang.	Ori.	T_p (s)	PGV (cm/s)	PI
1	3123	133.1	1.5	6	19	2.6	172.8	14.4	7	18	2.6	179.2	20.0	81	−56	3.6	51.0	3.8	87	−62	7.6	48.5	6.9
2	2712	32.8	1.7	56	−31	7.0	128.3	7.1	56	−31	7.1	126.7	7.5	82	−57	5.2	133.6	35.7	82	−57	6.6	109.0	25.2
3	2718	44.6	1.8	76	−79	6.0	134.0	7.9	76	−79	6.0	114.4	23.1	89	−66	6.5	105.4	26.8	83	−58	6.8	92.7	19.3
4	3145	82.9	1.8	49	74	4.2	147.5	23.0	50	75	4.2	147.9	24.4	82	−57	7.3	134.0	37.0	84	−59	5.1	78.3	15.3
5	4616	34.5	1.9	74	−49	8.4	104.9	10.9	70	−50	8.4	102.2	11.9	75	−50	5.1	126.7	19.5	73	−48	5.1	180.5	33.9
6	3138	64.6	2.1	47	72	7.9	184.3	12.3	49	74	7.5	173.2	25.0	75	−80	6.0	253.5	36.5	79	−76	4.5	127.8	19.9
7	3144	69.5	2.1	32	57	8.3	153.9	11.9	32	57	8.3	145.4	15.0	78	−77	5.9	245.0	42.1	81	−74	5.1	112.5	24.7
8	3131	134.9	2.3	54	−29	8.0	57.2	1.0	54	−29	7.9	59.8	4.6	89	−64	3.7	61.3	9.1	87	−62	5.5	49.9	9.2
9	2708	39.9	2.6	90	−65	3.2	172.4	5.2	89	−66	3.1	155.4	15.9	86	−61	5.8	150.3	43.3	87	−62	6.6	119.9	32.3
10	3143	58.5	3.1	73	−48	7.2	165.6	20.9	72	−47	7.3	157.6	24.6	83	−72	5.7	200.1	34.5	85	−70	3.7	99.8	1.9
11	4615	31.5	3.6	46	−21	5.5	166.0	23.9	48	−20	5.6	156.6	27.8	79	−54	3.3	68.6	3.0	−	−	−	−	−
12	3139	87.3	4.0	43	−18	3.1	151.8	19.8	43	−18	3.0	149.6	23.3	83	−72	7.7	158.2	15.9	87	−62	6.0	104.1	16.9
13	3142	97.2	4.1	89	−66	13.8	80.7	2.5	88	−67	13.5	77.1	0.6	66	−89	8.9	98.1	10.0	88	−67	3.9	91.7	16.4
14	NAR	32.5	4.2	28	53	4.8	125.7	19.2	25	53	4.8	121.8	20.8	−	−	−	−	−	−	−	−	−	−
15	KHMN	32.5	4.2	39	64	5.2	99.1	8.3	31	56	4.8	120.9	20.0	−	−	−	−	−	−	−	−	−	−
16	3137	74.2	4.8	58	−33	9.3	103.3	18.5	58	−33	9.2	98.5	18.5	85	−60	6.3	233.2	39.1	89	−66	5.5	121.4	28.9
17	3136	137.8	12.1	87	−62	11.5	58.1	1.7	87	−62	13.5	56.9	1.4	77	−78	4.5	57.6	6.1	82	−73	5.0	47.9	7.8
18	2715	50.1	12.6	87	−68	7.0	76.2	0.5	87	−68	6.6	56.8	13.3	−	−	−	−	−	−	−	−	−	−
19	2716	49.9	12.8	84	−59	6.9	73.5	7.5	84	−59	6.8	71	8.9	−	−	−	−	−	−	−	−	−	−
20	2717	49.8	13.0	86	−69	7.0	62.9	10.5	86	−69	6.9	60.6	11.6	−	−	−	−	−	−	−	−	−	−
21	8002	46.2	13.4	86	−61	9.2	42.8	3.3	86	−61	9.0	41.4	3.8	72	−47	6.1	75.4	14.7	75	−50	10.3	67.4	12.4
22	3116	97.9	14.8	0	25	15.1	49.9	7.1	1	26	14.4	47.5	6.4	66	−89	9.0	54.5	10.3	42	67	8.9	36.9	4.3
23	3134	85.2	24.9	77	−52	11.9	50.7	5.2	75	−50	11.7	48.7	4.2	83	−58	9.0	46.0	4.9	74	−49	7.9	37.4	1.4

R_{hypo} indicates the distance to the hypocenter; R_{rup} indicates the distance to the rupture plane; Ang. indicates the angle to the fault-parallel component; Ori. indicates the orientation of the strongest observed pulse, in degrees clockwise from north; PGV indicates the peak ground velocity of the strongest observed pulse; and T_p indicates the period of the extracted pulse in the direction of the strongest observed pulse.

Table 2. Parameters table of the extracted pulses for the Mw 7.5 Elbistan earthquake

Index	Sta.	R_{hypo} (km)	R_{rup} (km)	Uncorrected data					Corrected data				
				Ang.	Ori.	T_p (s)	PGV (cm/s)	PI	Ang.	Ori.	T_p (s)	PGV (cm/s)	PI
24	4612	64.0	3.0	87	−17	6.2	181.4	13.9	88	−18	6.2	180.9	13.7
25	131	97.7	15.4	76	−34	12.2	38.2	3.8	76	−34	11.7	37.4	4.0
26	132	97.7	15.5	87	−23	12	25.1	1.3	87	−23	11.8	24.2	1.0
27	4611	33.1	27.4	22	74	11	42.5	4.5	22	74	10.8	40.3	4.3
28	4614	61.3	55.9	10	86	9.3	34.2	3.5	11	86	9.3	34.5	3.7
29	NAR	71.1	68.2	6	90	9.7	27.9	2.6	7	89	9.6	26.5	2.2
30	4615	71.8	69.1	13	83	9.4	30.8	3.3	13	83	9.4	30.4	3.3

short distances, suggesting that the number of such false-positive impulsive motions remains limited.

Understanding the variability of pulse orientations

Somerville et al. (1997) showed that pulses can be present in two horizontal orthogonal components associated with two different phenomena (directivity effects and fling step) and can also overlap in some orientations. However, the static displacements are removed in the corrected data, excluding the fling-step effect from this dataset. Notably, the pulse orientation here indicates the orientation of the strongest pulse, representing the most dominant effect.

Figure 4 shows a comparison of pulse orientations and their uncertainty from the uncorrected data, corrected data, and first synthetic data. The within-pulse uncertainty in orientations ranges from 20 to 30 degrees in both observed and synthetic data. The orientations between pulses exhibit high variability in the observed data. However, the orientations of the synthetic data show that the pulses are predominantly aligned with the FN component, with less variability than the pulses from the observed data.

A common assertion is that near-field rupture directivity effects generate pulses in the FN component (Bray and Rodriguez-Marek, 2004; Kaneko and Goto, 2022; Somerville et al., 1997). However, the pulse orientations of these two events are highly variable, as shown in Figure 5a. The pulse orientations of the Pazarcik earthquake are highly variable in the near-fault region ($R_{rup} < 5$ km) but become more pronounced in the FN component for stations with $R_{rup} > 5$ km. At distant stations ($R_{rup} > 30$ km), the pulse orientations for the Elbistan earthquake are predominantly observed on the FP component. The pulses observed in this earthquake doublet demonstrate a large variability in orientations.

This significant variability in pulse orientation may not arise solely from directivity effects. Site effects (e.g. basin and soft-soil effects) may also influence the detected velocity pulses (Kobayashi et al., 2019). To analyze the site effect in this context, we evaluate the correlation between the pulse orientations and the corresponding Vs30 (a proxy for site conditions) (Figure 5b). A few pulses are observed at stations with low Vs30 (soft soils, Vs30 < 360 m/s). For these stations, pulses shown on the FP component may be a consequence of site effects (e.g. NAR). Ground motion pulses on soft soils would exhibit multiple large cycles in the time history, generally a signature of the presence of soft-soil effects (Somerville, 2003). The ground motion at station 3123 (Vs30 = 470 m/s) in the Pazarcik earthquake (showing a pulse-like feature) exhibits such multiple large cycles (Figure 5c).
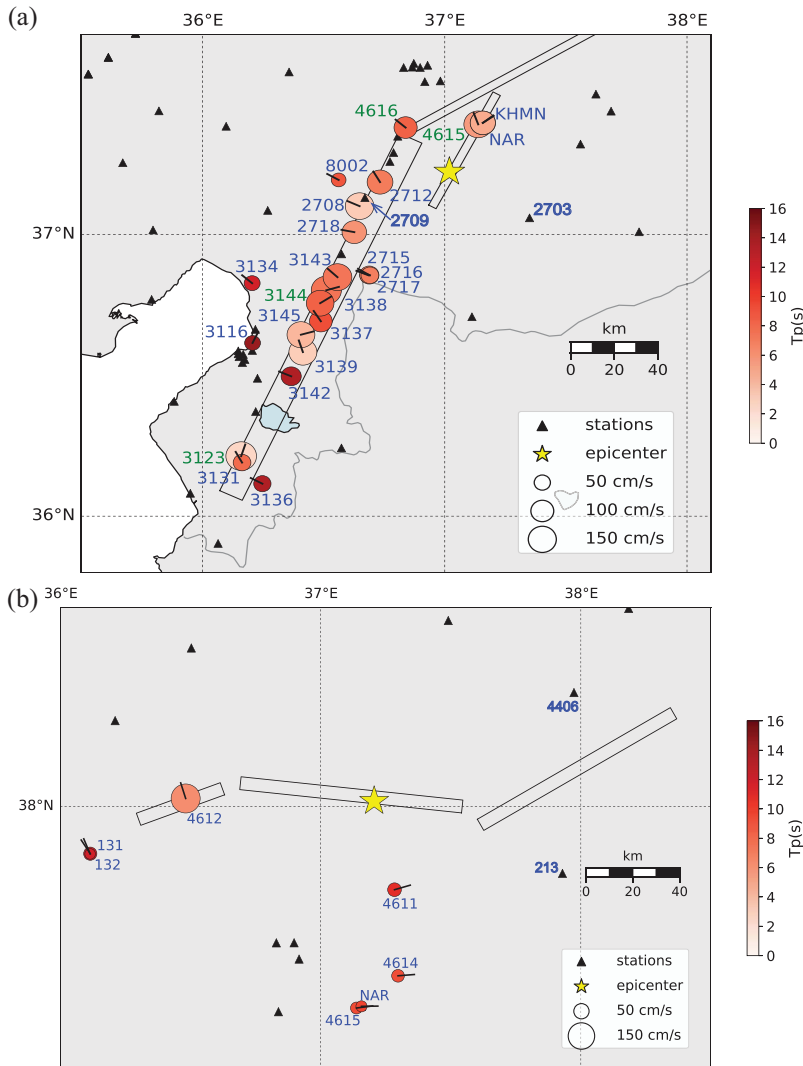
Figure 1. Distributions of the strongest velocity pulses detected for (a) the Mw 7.8 Pazarcik earthquake, and (b) the Mw 7.5 Elbistan earthquake from the corrected observation dataset. The circles represent the velocity pulses identified in the events. The size of the circles indicates the amplitude of the velocity pulses. The color of the circles represents the pulse period, T_p. The arrows on the circles indicate the orientations of the strongest pulses. Fault geometries are sourced from USGS. The station names highlighted in green are those shown in Figure 2, S1, and S2.

However, the correlation between pulse orientation and Vs30 remains weak, and most stations showing pulses are located on stiff soils, suggesting that other factors (see Discussion) may explain the variability in orientation.

Comparison of velocity pulses with a global dataset

In Figure 6, we compare the pulse periods extracted from the corrected data of this earthquake doublet with previously observed pulse periods from global earthquakes (Shahi and
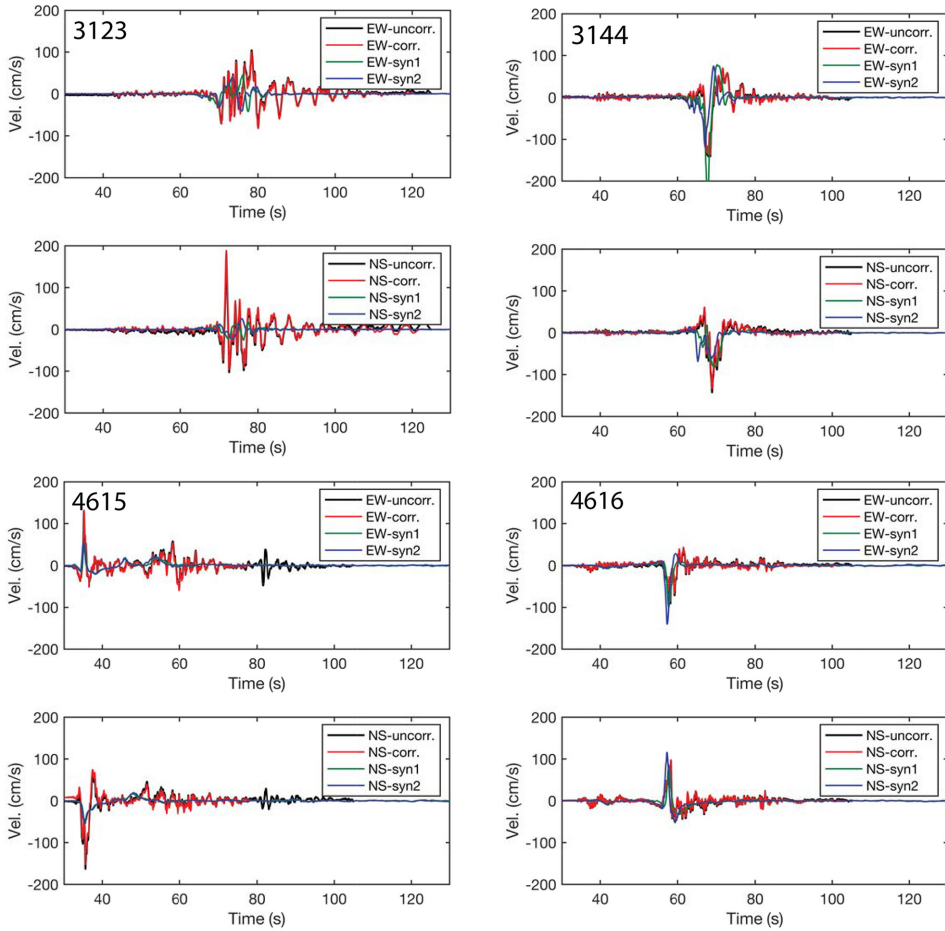
Figure 2. Comparison of velocity time histories on the EW and NS components for the uncorrected (uncorr.), corrected (corr.), first synthetic data (syn1), and second synthetic data (syn2) for the Mw 7.8 Pazarcik earthquake. The geographic locations of the stations (names in green) are shown in Figure 1.

Baker, 2014; Türker et al., 2023; Yen et al., 2022). Observations of earthquake pulses show a correlation between pulse period and earthquake magnitude, along with a large variability of pulse period for a single earthquake (various records of a single earthquake), as shown by Yen et al. (2022). The pulse periods observed in the Mw 7.5 Elbistan earthquake are comparable to those of the Mw 7.6 1999 Kocaeli earthquake.

Figure 7 illustrates the differences between the observed pulse periods and the predicted pulse periods calculated from the regression of Shahi and Baker (2014), revealing the differences to be substantial for large earthquakes (M > 7). The standard deviation (log transformation) of the pulse periods of the Mw 7.8 Pazarcik earthquake (1.19) is larger than that of the pulse periods of the Mw 7.5 Elbistan earthquake (0.64). This aligns with the findings of Yen et al. (2022), showing that variability of the pulse period for a single earthquake is magnitude-dependent (see Discussion).
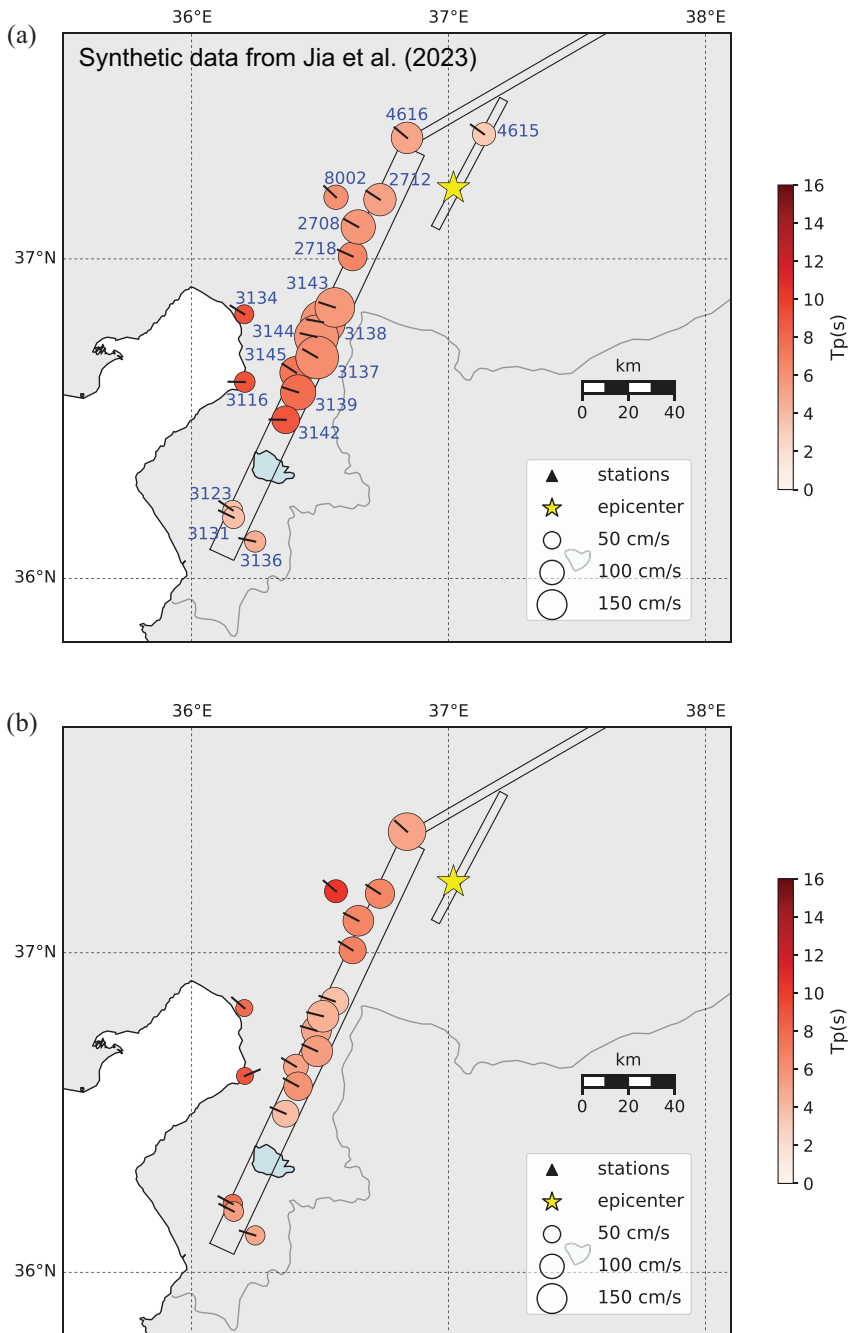
Figure 3. Distributions of the strongest velocity pulses detected from (a) simulations (Jia et al., 2023) and (b) simulations from the model of Jia et al. (2023) in higher resolution (numerically accurate to 5 Hz) for the Mw 7.8 Pazarcik earthquake. The circles represent the velocity pulses identified in the events. The size of the circles indicates the amplitude of the velocity pulses. The color of the circles represents the pulse period, T_p. The arrows on the circles indicate the orientations of the strongest pulses. Fault models are sourced from USGS geometries.
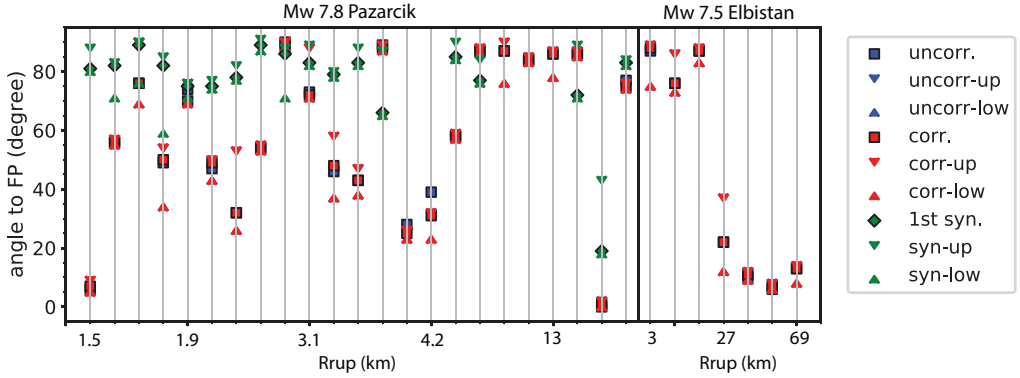
Figure 4. Comparison of the pulse orientations with the maximum and minimum values from the uncorrected data (blue squares), corrected data (red squares), and first synthetic data (green squares) of two earthquakes. The left panel displays the first event and the right panel the second event.

Table 3. The ratio of pulse-like motions over total stations per distance (D, km) bins.

	$0 < D \leqslant 10$	$10 < D \leqslant 20$	$20 < D \leqslant 50$
Empirical data	67%	50%	7%
First synthetics	58%	25%	7%
Second synthetics	54%	25%	7%

Since earlier studies have shown that the pulse period is not simply related to earthquake magnitude (Yen et al., 2022), we further analyze the correlation of the pulse period and PGV with the rupture distance, one of the dependencies contributing to this large variability (Figure 8). The pulse periods of the two events range from 3 to 14 s at different distances, suggesting no dependence between rupture distance and pulse period.

In Figure 8b, we compare the pulse PGV with the predicted PGV from the ground motion model of Bindi et al. (2014) for the Mw 7.8 earthquake, with a selected Vs30 = 480 m/s; the latter. The ground motion model of Bindi et al. (2014) is derived for Europe and the Middle East from the RESORCE strong motion database, which does not consider directivity effects. Notably, the predicted PGV is the geometric mean of the horizontal components, while the pulse PGV is the peak value of ground velocity projected along the extracted orientation. Generally, the pulse PGV is larger than the predicted PGV and around the upper bound of one standard deviation of the ground motion model predictions. In the near-fault regions ($R_{rup} < 5$ km), the largest pulse PGV reaches about 200 cm/s for the observations. This analysis confirms that the pulse PGV in the Pazarcik and Elbistan earthquakes is consistent with the values and decay with rupture distance shown by other earthquakes of similar magnitude.

Response spectra of pulse-like versus non-pulse-like recordings

While peak ground motion effectively represents the highest ground motion intensity during an earthquake, it cannot capture the seismic response of structures with distinct natural vibration periods when subjected to near-fault pulse-like ground motions. It is precisely
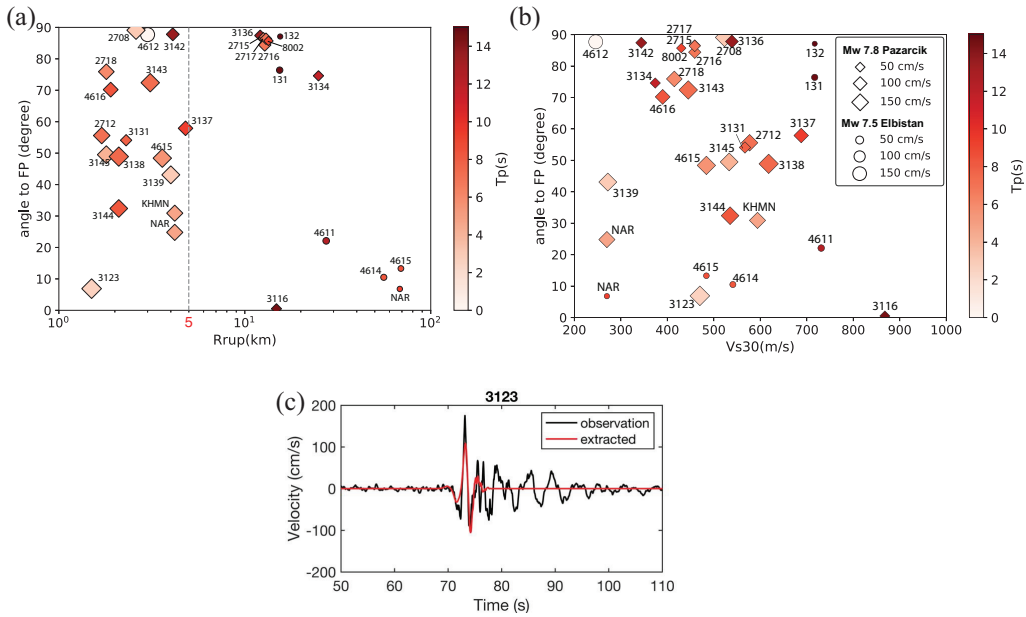
Figure 5. (a) Pulse periods, velocity, and angles to the FP component as a function of the rupture distance for the strongest pulses from the corrected data. (b) Pulse period, velocity, and angle to FP with Vs30 for the strongest pulses from the corrected data. The diamonds indicate the pulses of the Mw 7.8 Pazarcik earthquake while the circles depict the pulses of the Mw 7.5 Elbistan earthquake. The color represents the pulse periods. (c) A rotated time history of the pulse induced by the soft-soil effect at station 3123.

the amplitude and duration (T_p) of the seismic pulses that contribute to higher spectral displacement and may result in larger damage, depending on the structural behavior of the building (Güneş and Ulucan, 2019). The ratio of the pulse duration, T_p, to the natural period of the building, also known as the first mode period, T1, provides a critical parameter for describing structural response. Previous studies have demonstrated an expected wider shape in the acceleration response when near-fault ground motions include velocity pulses (Chopra and Chintanapakdee, 2001). Accordingly, the potential effects of near-fault pulse-like ground motions should be accounted for in probabilistic seismic hazard assessment (PSHA) studies, as suggested by Shahi and Baker (2011).

Considering the destructive and widespread damage caused by the two major events, we analyze the pseudo-elastic response spectra (hereafter referred to as response spectra) of several pulse-like and non-pulse-like recordings to evaluate the potential impacts of the detected velocity pulses on the seismic response of buildings. Figure 9 shows the velocity response spectra of pulse-like and non-pulse-like near-field recordings taken at similar fault distances ($R < 35$ km). The differences in the shape of the response spectra, as well as in the maximum values, are significant among the stations, with noticeably broader and higher spectral values for pulse-like recordings (red curves in Figure 9a). The pulse-like ground motion shakings are shifted to longer periods, posing a larger destruction potential for modern, taller buildings. This trend is more pronounced for the records of the Pazarcik event (Mw 7.8), as shown in Figure 9a. However, we emphasize that more stations are available for this event, unlike the Elbistan earthquake (Figure 9b), where only a handful
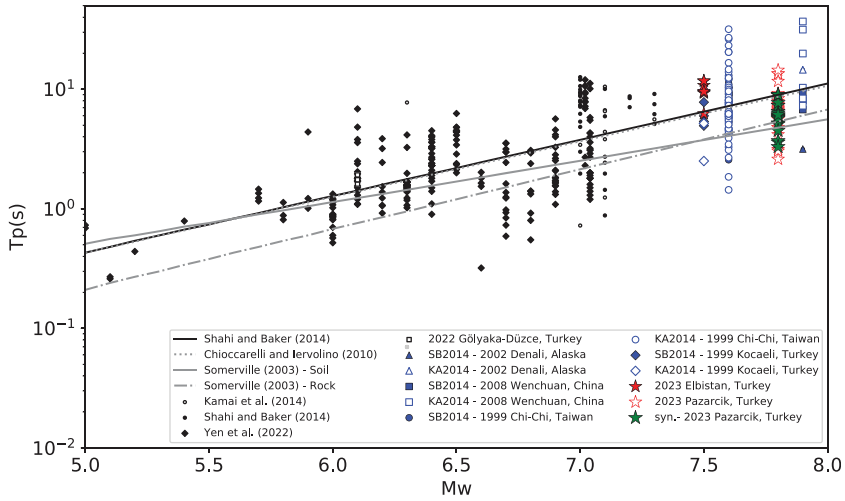
Figure 6. Values of the pulse period, T_p, as a function of earthquake moment magnitude. The lines show the regressions of Shahi and Baker (2014) (black solid line), Chioccarelli and Iervolino (2010) (gray dotted line), and Somerville (2003) (gray dashed-dotted-dashed line). Black dots represent the pulses identified from the NGA-West2 database (Ancheta et al., 2014) in the study of Shahi and Baker (2014). Open circles represent the fling-step pulses published by Kamai et al. (2014). Figure modified and adapted from Yen et al. (2022). Red stars represent the pulses of this earthquake doublet, while green stars represent the pulses of this earthquake doublet from the first synthetic data.
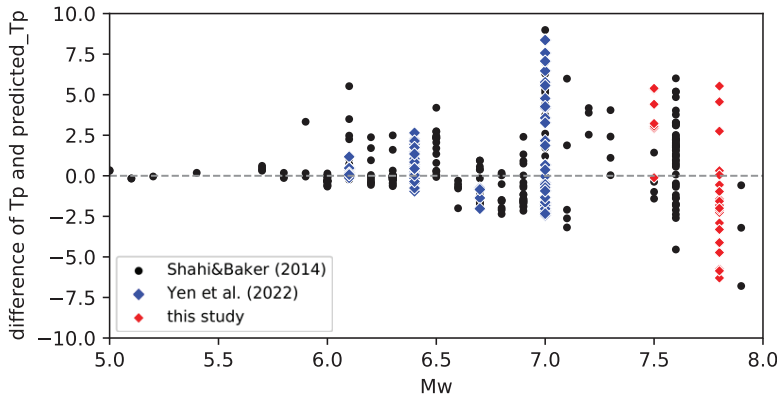
Figure 7. Differences between the observed pulse period and the predicted pulse period calculated from the regression of Shahi and Baker (2014).

of near-fault recordings are available. Such results are consistent with the analysis of Ertuncay and Costa (2024).

Discussion

In this study, we detect several velocity pulses near the ruptured fault segments ($R_{rup} = 1$–70 km) that strongly affect the response spectral characteristics of the observed ground

(a)

(b)
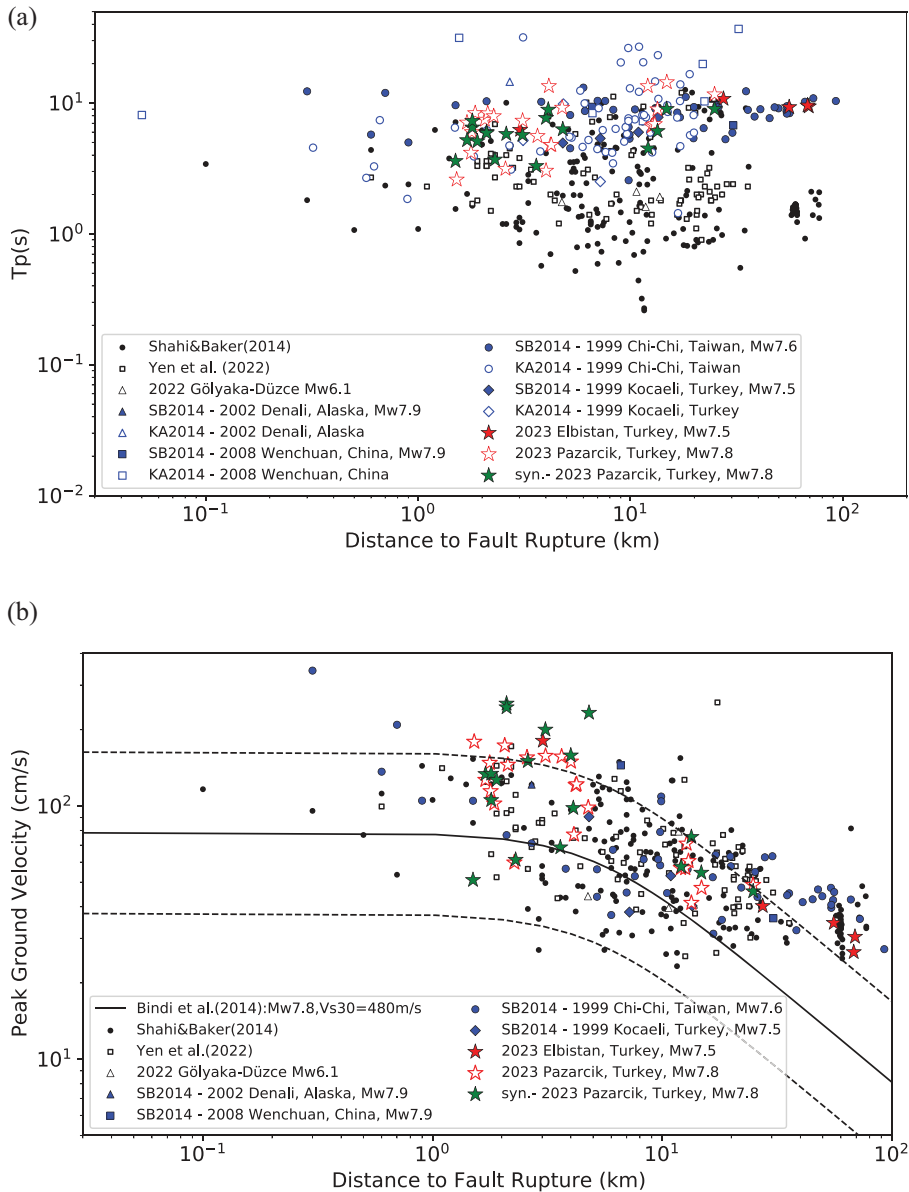
Figure 8. Scaling of (a) pulse period, T_p, and (b) pulse PGV, as a function of distance to fault rupture. Black dots represent the pulses identified from the NGA-West2 database (Ancheta et al., 2014) in the study by Shahi and Baker (2014) for M < 7.5 earthquakes. Open squares indicate the pulses published by Yen et al. (2022) for which the static offset of the events has been removed. The solid line in (b) represents the predicted ground velocities from the ground motion model of Bindi et al. (2014) for Mw 7.8 and Vs30 = 480 m/s. The dashed lines represent one standard deviation of the median of the predicted ground velocities.

motions (Figure 9). Comparisons of pulse period and pulse velocity amplitude with other damaging earthquakes in global datasets confirm that the pulses of these two events are not unexpectedly large and are consistent with past observations (Figures 6 and 8).
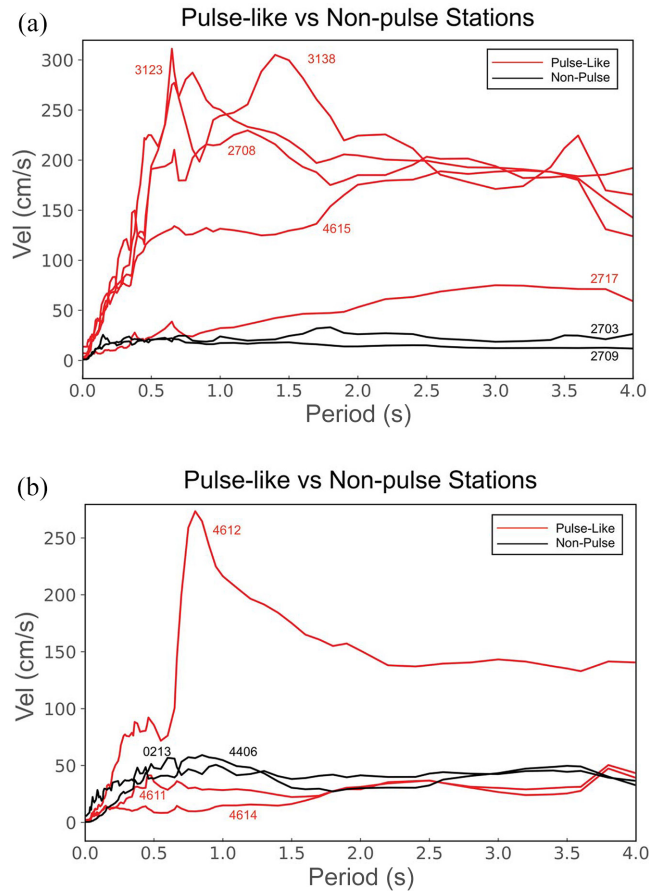
Figure 9. A selection of velocity response spectra of the observations for the strong pulses (PI > 10) for (a) the Mw 7.8 Pazarcik and (b) the Mw 7.5 Elbistan earthquakes. Red curves show the velocity response spectra of stations with a pulse-like feature, while black curves show the velocity response spectra of stations without a pulse-like feature.

The pulses observed during the Mw 7.8 Pazarcik earthquake exhibit large variability in pulse characteristics, even when fling-step effects are excluded (Figure 1). The occurrence of the pulses is highly specific to the station location. Indeed, variation of the pulse properties remains significant even when the inter-station distance (D) is small (D < 5 km). For example, in the Pazarcik earthquake, stations 2708 and 2709 are close to each other (D = 3.8 km), but the record of only one station was defined as pulse-like (Figure 1). There is a substantial difference in pulse orientation (73°) between station 4615 and NAR (D = 1.8 km) (Table 1).

In the empirical regressions of pulse period and earthquake magnitude, standard deviations are calculated for all events. However, our results reveal that the differences between the observed and predicted pulse periods from the regression of Shahi and Baker (2014) are large for large earthquakes. This is consistent with the finding of Yen et al. (2022) that the standard deviation of the pulse period in a single earthquake is indeed magnitude-dependent. Large earthquakes may involve more complex physical phenomena, such as

more heterogeneous slip and varied fault mechanisms, contributing to increased pulse variability. Consequently, this magnitude-dependent variability suggests the importance of further investigation into the driving factors of pulse variability between earthquakes.

Several studies over the last few decades have focused on directivity pulses due to their destructive nature. Somerville et al. (1997) showed that directivity pulses are often expected on the FN component for strike-slip earthquakes. However, Poulos and Miranda (2023) and Türker et al. (2023) found that the orientations of the maximum spectral response (i.e. pulse orientation) do not occur exclusively on the strike-normal orientation when considering stations recorded at different distances. The results of our study support these observations, as the two events exhibit highly variable pulse orientations, with no tendency to align solely on the FN component (Figure 5). The kinematic simulations (Figure S3) indicate that pulse orientations depend strongly on the faulting mechanism and the location of the station relative to the fault in the near-fault region. This is consistent with the finding of Poiata et al. (2017), which indicated that pulses are influenced not only by directivity effects but also by a combination of rupture configurations and the S-wave radiation pattern.

Another interpretation is that the presence of directivity pulses is strongly related to slip heterogeneity on the fault plane, where the location and size of asperities (large slip areas) determine the generation of directivity pulses (Mena and Mai, 2011). Dreger et al. (2011) simulated strong ground motions using a 3D finite-difference method and found that segmented faults and short-wavelength variations in fault geometry can introduce complexity that affects the degree of directivity focusing and the FP motions. Their simulations indicate that both fling steps and directivity pulses can occur in any of the three components and suggest that faulting style and variations in fault parameters must be considered in detailed site-specific analyses. Horizontal polarities of near-field ground motion also reflect the dynamic complexities of rupture, such as sub-shear versus supershear rupture speeds (Ben-Zion et al., 2024). This suggests that dynamic rupture simulations should consider more heterogeneous slip, faulting mechanisms, or fault geometry complexity to reproduce the variability of pulse observations.

Some studies have also found that site effects can influence both the amplitude and the period of directivity pulses when the pulse period is close to the site resonance period (Kobayashi et al., 2019; Rodriguez-Marek and Bray, 2006). Our analysis of pulse orientations and the correlation with Vs30 and the ground motion at station 3123 (Figure 5c) confirms that site effects, together with directivity effects, can affect pulse characteristics, specifically increasing its amplitude. However, site effects are possibly not the main controlling factors since the correlation with Vs30 remains weak (Figure 5). Other factors mentioned above (e.g. heterogeneous slip and complexity of faulting dynamics and geometry) may contribute more to pulse variability in this earthquake doublet.

In this study, we assume the accuracy of the orientations provided in the ESM database. However, Büyükakpınar et al. (2021) reported temporal changes in the sensor orientation of some stations in the Kandilli Observatory and Earthquake Research Institute (KOERI) network. To our knowledge, such sensor orientation errors have not been detected for the stations used in this study. If such misorientation of the sensor components exists, it may potentially cause bias in the variability of the observed pulse orientation.

Conclusion

In this study, we demonstrate that pulse characteristics, particularly the pulse orientation, in the near-fault regions of large-magnitude earthquakes can be highly variable and that the variability of the pulse period for a single earthquake is magnitude-dependent, as found by Yen et al. (2022). This pronounced variability in pulse characteristics can be attributed to diverse factors (e.g. directivity, site, and source effects). We confirm that site effects can amplify pulse amplitude when the pulse period is close to the site resonance frequency, as observed at station 3123 in the Mw 7.8 Pazarcik earthquake. However, site effects are not the primary factor in increasing pulse variability. Our results also suggest that heterogeneous slip and more complex faulting dynamics are major contributors to increased pulse variability in large earthquakes and that the interaction of these factors further complicates pulse properties. The significant pulse variability resulting from various driving factors emphasizes the importance of studying each earthquake individually to understand the factors influencing pulse characteristics.

ORCID iD

Ming-Hsuan Yen (iD) https://orcid.org/0000-0002-4613-4835

Data and resources

Preliminary finite fault geometry from the USGS: M7.8 Pazarcik earthquake "https://earthquake.usgs.gov/earthquakes/eventpage/us6000jllz/finite-fault" and M7.5 Elbistan earthquake "https://earthquake.usgs.gov/earthquakes/eventpage/us6000jlqa/finite-fault" (last accessed 20/06/2023). ESM

Ground motion records: https://esm-db.eu/ (last accessed 20/06/2023). The raw data from AFAD: https://en.afad.gov.tr/ (last accessed 31/03/2023).

Supplemental material

Supplemental material for this article is available online.

References

Ancheta TD, Darragh RB, Stewart JP, Seyhan E, Silva WJ, Chiou BS-J, Wooddell KE, Graves RW, Kottke AR, Boore DM, Kishida T and Donahue JL (2014) NGA-West2 database. *Earthquake Spectra* 30(3): 989–1005.

Baltzopoulos G, Baraschino R, Chioccarelli E, Cito P, Vitale A and Iervolino I (2023) Near-source ground motion in the M7.8 Gaziantep (Turkey) earthquake. *Earthquake Engineering & Structural Dynamics* 52(12): 3903–3912.

Ben-Zion Y, Zhang S and Meng X (2024) Isotropic high-frequency radiation in near-fault seismic data. *Geophysical Research Letters* 51(17): e2024GL110303.

Bindi D, Massa M, Luzi L, Ameri G, Pacor F, Puglia R and Augliera P (2014) Pan-European ground-motion prediction equations for the average horizontal component of PGA, PGV, and 5 %-damped PSA at spectral periods up to 3.0 s using the RESORCE dataset. *Bulletin of Earthquake Engineering* 12(1): 391–430.

Bray JD and Rodriguez-Marek A (2004) Characterization of forward-directivity ground motions in the near-fault region. *Soil Dynamics and Earthquake Engineering* 24(11): 815–828.

Büyükakpınar P, Aktar M, Maria Petersen G and Köseoğlu A (2021) Orientations of broadband stations of the KOERI seismic network (Turkey) from two independent methods: P- and Rayleigh-wave polarization. *Seismological Research Letters* 92(3): 1512–1521.

Chioccarelli E and Iervolino I (2010) Near-source seismic demand and pulse-like records: A discussion for L'Aquila earthquake. *Earthquake Engineering & Structural Dynamics* 39(9): 1039–1062.

Chopra AK and Chintanapakdee C (2001) Comparing response of SDF systems to near-fault and far-fault earthquake motions in the context of spectral regions. *Earthquake Engineering & Structural Dynamics* 30(12): 1769–1789.

Dreger D, Hurtado G, Chopra A and Larsen S (2011) Near-field across-fault seismic ground motions. *Bulletin of the Seismological Society of America* 101(1): 202–221. DOI: 10.1785/0120090271

Duman TY and Emre Ö (2013) The East Anatolian Fault: Geometry, segmentation and jog characteristics. *Geological Society, London, Special Publications* 372(1): 495–529.

Erdik M, Tümsa MBD, Pınar A, Altunel E and Zülfikar AC (2023) A preliminary report on the February 6, 2023 earthquakes in Türkiye. Available at: http://doi.org/10.32858/temblor.297

Ertuncay D and Costa G (2024) Analysis of impulsive ground motions from the February 2023 Kahramanmaraş earthquake sequence. *Bulletin of Earthquake Engineering*. Epub ahead of print 2 April. DOI: 10.1007/s10518-024-01897-x.

Gabriel A, Ulrich T, Marchandon M, Biemiller J and Rekoske J (2023) 3D dynamic rupture modeling of the 6 february 2023, Kahramanmaraş, Turkey Mw 7.8 and 7.7 earthquake doublet using early observations. *The Seismic Record* 3(4): 342–356.

Güneş N and Ulucan ZÇ (2019) Nonlinear dynamic response of a tall building to near-fault pulse-like ground motions. *Bulletin of Earthquake Engineering* 17(6): 2989–3013.

Güvercin SE, Karabulut H, Konca AÖ, Doğan U and Ergintav S (2022) Active seismotectonics of the East Anatolian Fault. *Geophysical Journal International* 230(1): 50–69.

Hacettepe University, Department of Civil Engineering (2023) 06 February 2023—Kahramanmaraş Pazarcık (Mw = 7.7) and Kahramanmaraş Elbistan (Mw = 7.6) report on the investigation of earthquakes. *Hacettepe University Department of Civil Engineering Report*. Available at: https://drive.google.com/file/d/1u8LYtSvkks53iVImuflrzw1weHEDKZhk/view?pli = 1

Heaton TH, Hall JF, Wald DJ and Halling MW (1995) Response of high-rise and base-isolated buildings to a hypothetical Mw 7.0 blind thrust earthquake. *Science* 267(5195): 206–211.

Hisada Y and Tanaka S (2021) What is fling step? Its theory, simulation method, and applications to strong ground motion near surface fault ruptures. *Bulletin of the Seismological Society of America* 111(5): 2486–2506.

Jia Z, Jin Z, Marchandon M, Ulrich T, Gabriel A-A, Fan W, Shearer P, Zou X, Rekoske J, Bulut F, Garagon A and Fialko Y (2023) The complex dynamics of the 2023 Kahramanmaraş, Turkey, Mw 7.8-7.7 earthquake doublet. *Science* 381(6661): 985–990.

Kamai R, Abrahamson N and Graves R (2014) Adding fling effects to processed ground-motion time histories. *Bulletin of the Seismological Society of America* 104(4): 1914–1929. DOI: 10.1785/0120130272

Kaneko Y and Goto H (2022) The origin of large, long-period near-fault ground velocities during surface-breaking strike-slip earthquakes. *Geophysical Research Letters* 49(10): e2022GL098029.

Kobayashi H, Koketsu K and Miyake H (2019) Rupture process of the 2018 Hokkaido Eastern Iburi earthquake derived from strong motion and geodetic data. *Earth, Planets and Space* 71(1): 63.

Lin Y-Y, Kanamori H, Zhan Z, Ma K-F and Yeh T-Y (2020) Modelling of pulse-like velocity ground motion during the 2018 Mw 6.3 Hualien earthquake, Taiwan. *Geophysical Journal International* 223(1): 348–365.

Luzi L, Lanzano G, Felicetta C, D'Amico MC, Russo E, Sgobba S and Pacor F; ORFEUS Working Group 5 (2020) Engineering Strong Motion Database (ESM) (Version 2.0). *Istituto Nazionale di Geofisica e Vulcanologia (INGV)*. Available at: https://doi.org/10.13127/ESM.2

Mai PM, Aspiotis T, Aquib TA, Cano EV, Castro Cruz D, Espindola Carmona A, Li B, Li X, Liu J, Matrau R, Nobile A, Palgunadi KH, Ribot M, Parisi L, Suhendi C, Tang Y, Bora Y, Avşar U, Klinger Y and Jónsson S (2023) The destructive earthquake doublet of 6 February 2023 in South-Central Türkiye and Northwestern Syria: Initial observations and analyses. *The Seismic Record* 3(2): 105–115.

Mena B and Mai PM (2011) Selection and quantification of near-fault velocity pulses owing to source directivity. *Georisk: Assessment and Management of Risk for Engineered Systems and Geohazards* 5(1): 25–43.

Miyake H, Koketsu K, Hikima K, Shinohara M and Kanazawa T (2010) Source fault of the 2007 Chuetsu-oki, Japan, Earthquake. *Bulletin of the Seismological Society of America* 100(1): 384–391.

Paolucci R, Pacor F, Puglia R, Ameri G, Cauzzi C and Massa M (2011) Record processing in ITACA, the New Italian strong-motion database. *Earthquake Data in Engineering Seismology, Geotechnical, Geological, and Earthquake Engineering* 14: 99–113.

Petersen GM, Büyükakpinar P, Vera Sanhueza FO, Metz M, Cesca S, Akbayram K, Saul J and Dahm T (2023) The 2023 Southeast Türkiye seismic sequence: Rupture of a complex fault network. *Seismic Record* 3(2): 134–143.

Poiata N, Miyake H and Koketsu K (2017) Mechanisms for generation of near-fault ground motion pulses for dip-slip faulting. *Pure and Applied Geophysics* 174: 3521–3536.

Poulos A and Miranda E (2023) Effect of style of faulting on the orientation of maximum horizontal earthquake response spectra. *Bulletin of the Seismological Society of America* 113(5): 2092–2105.

Rodriguez-Marek A and Bray JD (2006) Seismic site response for near-fault forward directivity ground motions. *Journal of Geotechnical and Geoenvironmental Engineering* 132(12): 1611–1620.

Schliwa N and Gabriel A (2023) Equivalent near-field corner frequency analysis of 3D dynamic rupture simulations reveals dynamic source effects. *Seismological Research Letters* 95(2A): 900–924.

Sengör AMC, Gorur N and Saroglu F (1985) Strike-slip faulting and related basin formation in Zoneszones of tectonic escape: Turkey as a case study. *Society of Economic Paleontologists and Mineralogists, Special Publication* 37: 227–264.

Shahi SK and Baker JW (2011) An empirically calibrated framework for including the effects of near-fault directivity in probabilistic seismic hazard analysis. *Bulletin of the Seismological Society of America* 101(2): 742–755.

Shahi SK and Baker JW (2014) An efficient algorithm to identify strong-velocity pulses in multicomponent ground motions. *Bulletin of the Seismological Society of America* 104(5): 2456–2466.

Somerville PG (2003) Magnitude scaling of the near fault rupture directivity pulse. *Physics of the Earth and Planetary Interiors* 137(1): 201–212.

Somerville PG, Smith NF, Graves RW and Abrahamson NA (1997) Modification of empirical strong ground motion attenuation relations to include the amplitude and duration effects of rupture directivity. *Seismological Research Letters* 68(1): 199–222.

Strasser FO and Bommer JJ (2009) Review: Strong ground motions—have we seen the worst? *Bulletin of the Seismological Society of America* 99(5): 2613–2637.

Tatar O, Piper JDA, Gürsoy H, Heimann A and Koçbulut F (2004) Neotectonic deformation in the transition zone between the dead sea transform and the East Anatolian Fault Zone, Southern Turkey: A palaeomagnetic study of the Karasu Rift Volcanism. *Tectonophysics* 385(1-4): 17–43.

Türker E, Yen M, Pilz M and Cotton F (2023) Significance of pulse-like ground motions and directivity effects in moderate earthquakes: The example of the Mw 6.1 Gölyaka-Düzce earthquake on 23 november 2022. *Bulletin of the Seismological Society of America* 114(2): 955–964.

Wang Y and Day SM (2020) Effects of off-fault inelasticity on near-fault directivity pulses. *Journal of Geophysical Research: Solid Earth* 125(7): e2019JB019074.

Yen M-H, von Specht S, Lin Y-Y, Cotton F and Ma K-F (2022) Within- and between-event variabilities of strong-velocity pulses of moderate earthquakes within dense seismic arrays. *Bulletin of the Seismological Society of America* 112(1): 361–380.

Zhu L and Rivera LA (2002) A note on the dynamic and static displacements from a point source in multilayered media. *Geophysical Journal International* 148(3): 619–627.